

# Quantification of Heterogeneous Degradation in Li-Ion Batteries

Yang Yang, Rong Xu, Kai Zhang, Sang-Jun Lee, Linqin Mu, Pengfei Liu, Crystal K. Waters, Stephanie Spence, Zhengrui Xu, Chenxi Wei, David J. Kautz, Qingxi Yuan, Yuhui Dong, Young-Sang Yu, Xianghui Xiao, Han-Koo Lee, Piero Pianetta, Peter Cloetens, Jun-Sik Lee, Kejie Zhao,\* Feng Lin,\* and Yijin Liu\*

The multiscale chemomechanical interplay in lithium-ion batteries builds up mechanical stress, provokes morphological breakdown, and leads to state of charge heterogeneity. Quantifying the interplay in complex composite electrodes with multiscale resolution constitutes a frontier challenge in precisely diagnosing the fading mechanism of batteries. In this study, hard X-ray phase contrast tomography, capable of nanoprobng thousands of active particles at once, enables an unprecedented statistical analysis of the chemomechanical transformation of composite electrodes under fast charging conditions. The damage heterogeneity is demonstrated to prevail at all length scales, which stems from the unbalanced electron conduction and ionic diffusion, and collectively leads to the nonuniform utilization of active particles spatially and temporally. This study highlights that the statistical mapping of the chemomechanical transformation offers a diagnostic method for the particles utilization and fading, hence could improve electrode formulation for fast-charging batteries.

rechargeable batteries. Efforts have been devoted to studying different battery components (e.g., cathode, anode, electrolyte, and binder), aiming to improve energy and power densities, enhance safety, prolong lifetime, and reduce cost. An important aspect of the battery research is to identify the fading pathways of battery particles and electrodes at multiple length/time scales under practical operating conditions.<sup>[1]</sup> Redox reactions in batteries commonly involve phase transformation, lattice volume change, stress buildup, grain boundary weakening, and particle fracturing. These processes intertwine at multiple length and time scales, are termed as the chemomechanical interplay, and contribute to the complex fading mechanisms of composite battery electrodes. Mapping the chemomechanical

transformation of battery particles and particle ensembles represents a promising methodology to establish the relationship among all these processes. Such a study will potentially provide insights into designing materials and electrodes where

## 1. Introduction

The rapidly growing market for consumer electronics and electric vehicles has motivated tremendous ongoing researches in

Dr. Y. Yang, Dr. P. Cloetens  
ESRF-The European Synchrotron  
Grenoble 38043, France

Dr. R. Xu, P. Liu, Prof. K. Zhao  
School of Mechanical Engineering  
Purdue University  
West Lafayette, IN 47907, USA  
E-mail: kjzhao@purdue.edu

Dr. K. Zhang, Dr. Q. Yuan, Dr. Y. Dong  
Beijing Synchrotron Radiation Facility  
Institute of High Energy Physics  
Chinese Academy of Science  
Beijing 100049, China

Dr. K. Zhang, Dr. S.-J. Lee, C. Wei, Dr. H.-K. Lee, Prof. P. Pianetta,  
Dr. J.-S. Lee, Dr. Y. Liu  
Stanford Synchrotron Radiation Lightsource  
SLAC National Accelerator Laboratory  
Menlo Park, CA 94025, USA  
E-mail: liuyijin@slac.stanford.edu

Dr. L. Mu, C. K. Waters, S. Spence, Z. Xu, D. J. Kautz, Prof. F. Lin  
Department of Chemistry  
Virginia Tech  
Blacksburg, VA 24061, USA  
E-mail: fenglin@vt.edu

Dr. Y.-S. Yu  
Advanced Light Source  
Lawrence Berkeley National Laboratory  
Berkeley, CA 94720, USA

Dr. X. Xiao  
National Synchrotron Light Source II  
Brookhaven National Laboratory  
Upton, NY 11973, USA

Dr. H.-K. Lee  
Pohang Accelerator Laboratory  
Pohang 790-784, Republic of Korea

 The ORCID identification number(s) for the author(s) of this article can be found under <https://doi.org/10.1002/aenm.201900674>.

DOI: 10.1002/aenm.201900674

active particles can all be utilized to deliver full capacity, given its capability of drawing the spectrum of the chemomechanical interplay at length scales ranging from the nanometric scale, single particles, particle ensembles, to the electrode.

The metal oxide based intercalating battery chemistry represents an excellent platform to investigate the multiscale chemomechanical interplay. Nickel-rich layered materials,  $\text{LiNi}_{1-x-y}\text{Mn}_x\text{Co}_y\text{O}_2$  (NMC), are a promising cathode candidate for high energy density intercalating lithium-ion batteries.<sup>[2-4]</sup> They, however, suffer from the capacity fade, especially, when being charged to a high cutoff voltage, which is a necessary procedure to unleash the high energy density potential of the layered material.<sup>[5]</sup> Although all the transition metal elements in the NMC cathode undergo redox reactions upon cycling, different elements have different characteristics and, therefore, the NMC cathodes' performance varies significantly as a function of their compositions. Typical examples include the Li- and Mn-rich layered NMC<sup>[6]</sup> and the Ni-rich NMC.<sup>[7]</sup> The current trend of increasing Ni concentration (i.e., lowering Co/Mn contents) in NMCs further accentuates the need to understand and, subsequently, to enhance the structural and chemical stability of the polycrystalline nickel-rich NMC cathode. While the increment in Ni content offers more redox active Ni cations for the charge compensation during energy storage/release and, thus, favors high energy density, the reduction in Co and Mn content could harm the morphological integrity,<sup>[4]</sup> thermal robustness,<sup>[8]</sup> and lattice structural stability.<sup>[9,10]</sup> The chemomechanical interplay in nickel-rich NMC cathodes is an active research frontier.<sup>[11]</sup> The development of structural defects, that is, microcracks, is not only dependent on the global cathode composition<sup>[5]</sup> but also can be largely influenced by current density,<sup>[12,13]</sup> voltage window,<sup>[14]</sup> and temperature.<sup>[15-19]</sup> Advanced imaging methods, such as synchrotron-based X-ray probes,<sup>[20-26]</sup> scanning/transmission electron microscopy,<sup>[27-29]</sup> atomic force microscopy,<sup>[30]</sup> and micro-Raman mapping,<sup>[31]</sup> have been employed for in-depth investigations in this field. Among all these diagnostic tools, the X-ray probes with sufficient spatial resolution and compositional/chemical sensitivity show advantages of correlating the morphological and chemical features of the material. Particularly, when coupled with advanced computing methods for quantification<sup>[32-34]</sup> and modeling<sup>[24,35]</sup> of the data, the X-ray imaging methods have been demonstrated to be noninvasive, effective, and informative.

Here, we combine hard X-ray phase contrast nanotomography, transmission X-ray microscopy, nanoscale hard X-ray spectromicroscopy, soft X-ray absorption spectroscopy (XAS), and transmission electron microscopy (TEM) to systematically investigate the morphological and chemical degradation in polycrystalline nickel-rich layered NMC composite electrode under fast charging conditions. We visualize and quantify the degree of local damage in the composite electrode that is hierarchically complex. From the quantitative visualizations of the chemomechanical interplay, we have also extracted the depth-dependent trend of particle fracturing within the electrode as well as its lateral complexity. Finite element modeling (FEM) with shape models recovered from the nanotomography data is adopted to gain insights into the electrode level strain distribution and evolution. Our result features the statistical mapping of the chemomechanical transformation in the

composite electrode, which offers a diagnostic method for probing and understanding the nonuniform particles utilization and fading. We anticipate that the developed methodology and understanding will pave the way toward improved electrode formulation for fast-charging batteries.

## 2. Results and Discussion

### 2.1. The Cathode Particle's Structural Degradation at Multiscale

#### 2.1.1. The Cathode Particle's Structural Degradation at the Atomic Scale

We start with the atomic scale and show, in **Figure 1**, the TEM images over a cracked area on the chemically delithiated NMC622 ( $\text{Li}_x\text{Ni}_{0.6}\text{Mn}_{0.2}\text{Co}_{0.2}\text{O}_2$ ,  $x = 0.3$ ) cathode. The different atomic structures can be directly visualized in Figure 1a, in particular, over two highlighted regions of interest (ROI). The (inverse) fast Fourier transform analysis (Figure 1b-g) clearly supports the copresence of the layered and the rock salt phases over the localized region. The observed phase transformation from the layered to the rock salt structures can nucleate further development of microcracks that could propagate throughout the cathode particles, which will be discussed in Section 2.1.2.

#### 2.1.2. The Cathode Particle's Structural Degradation at the Mesoscale upon Fast Cycling

While the undesired local phase transformation is often considered as the root cause of the cathode degradation, the structural and chemical heterogeneity at the mesoscale further complicates the system.<sup>[26]</sup> At the mesoscale, the secondary particles of the NMC622 cathode are populated with grain boundaries and micropores, which not only influence the electrical and ionic transport in the system but also govern the propagation of the redox reaction fronts.<sup>[14]</sup> We employ nanoresolution X-ray spectromicroscopy<sup>[36]</sup> to visualize the microcracks and the corresponding chemical responses in a charged NMC622 particle after extensive cycling (50 cycles between 2.5 and 4.5 V at a rate of 5C). As shown in the 3D rendering of the particle morphology in Figure 1h, we could see a severe disintegration of the studied particle. The electrochemical cycling induced disintegration of NMC secondary particle can be attributed to the periodic lattice breathing and state of charge (SoC) heterogeneity.<sup>[37]</sup> There are a number of factors,<sup>[12]</sup> for example, the cycling rate, the cycling voltage window, the environmental temperature, the wettability of active particles, and the particle size and shape, which could influence the degree of the particle cracking.

The chemical sensitivity provided by the nanoresolution X-ray spectromicroscopy offers the opportunity to investigate the correlation between the mesoscale structural defects and the local chemical responses. We show in Figure 1i an *xy* slice through the center of the particle with the corresponding edge energy map (over the Ni K-edge) displayed in Figure 1j. A closer look suggests the coexistence of two types of microcracks in the NMC622 particle. Some of the cracks are well-developed

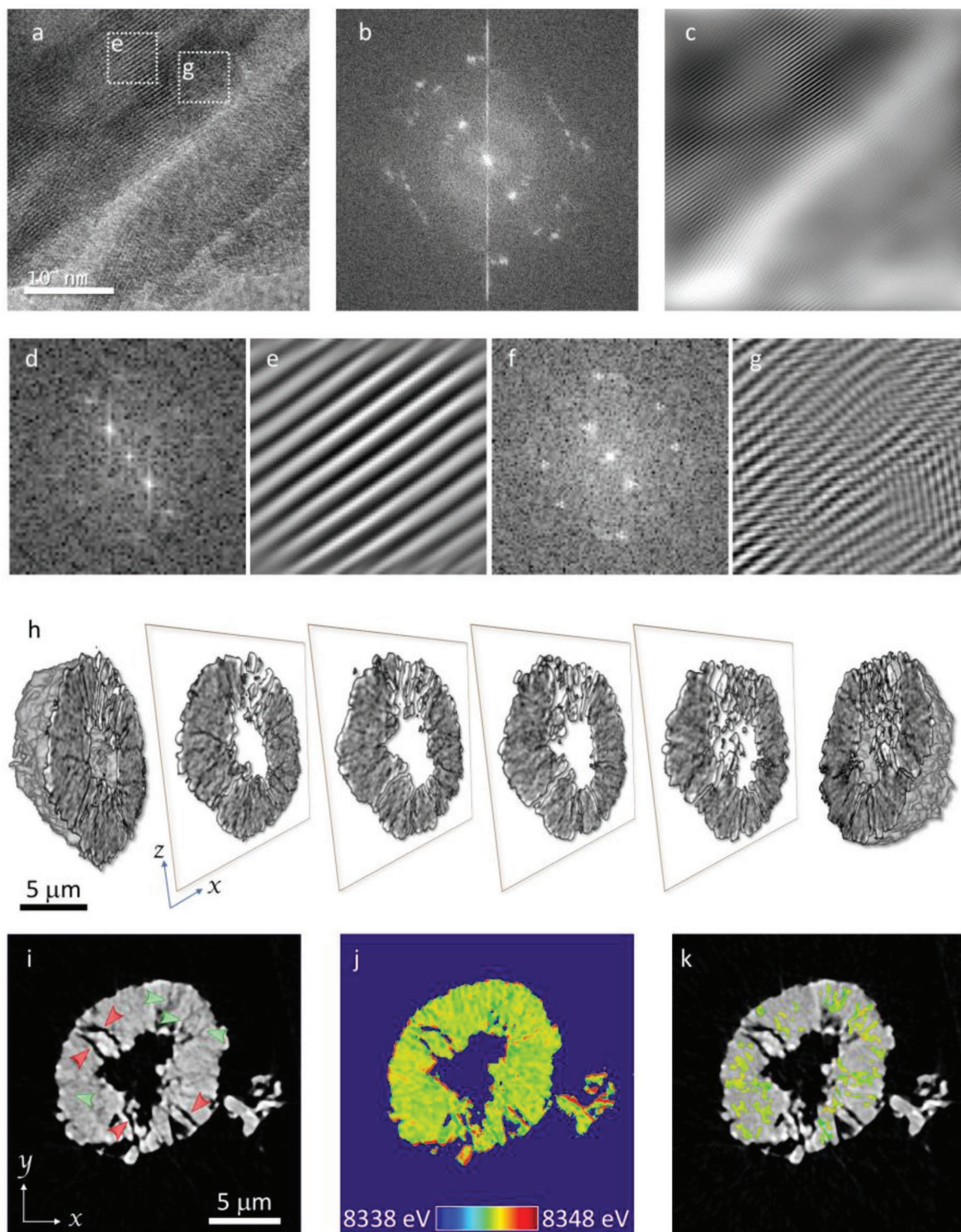


**Figure 1.** Structural defects in NMC622 at nano and mesoscales. a) A TEM image that reveals the mixed rock salt and layered structure along the region of local defects in the chemically delithiated NMC622. b,c) The fast Fourier transform (FFT) and inverse FFT (IFFT) of the entire high-resolution image (a), showing the copresence of layered and rock salt phases. d,f) The FFT and e,g) IFFT over selected regions of interest (ROI), showing the presence of layered and rock salt phases, respectively. The ROIs are marked as white-dotted squares in (a). h–k) The mesoscale structural and chemical degradation in electrochemically charged secondary NMC622 particles. h) The 3D rendering from X-ray spectromicroscopy results with a few  $xz$  slices through different positions displayed in the center. i) An  $xy$  slice through the center of the particle. Two different types of cracks, for example, the wide-open cracks (black regions; red arrows in (i)) and fine cracks (gray regions with lower contrast; green arrows in (i)), can be observed. j) The false-colored map (color map shown in the inset) of local Ni K-edge energy over the same  $xy$  slice in (i). k) The local edge energy over the fine cracks was segmented.

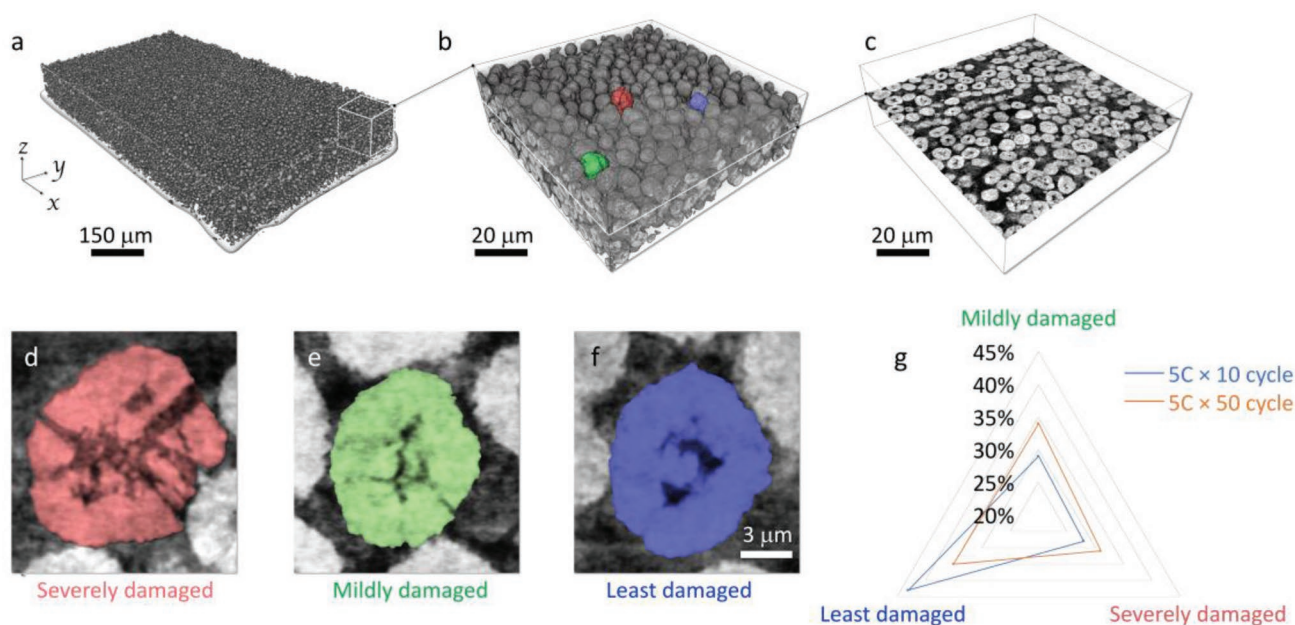


**Figure 2.** Multiple length scale X-ray tomographic imaging of NMC622 electrode. a) Microtomography (650 nm pixel size) data of a piece of NMC electrode. b) The 3D rendering of the nanotomography data (70 nm pixel size) of an arbitrarily selected region of interest over the electrode, c) with its central slice in the lateral direction. d–f) Three of the representative particles are highlighted in red, green, and blue. They are categorized as severely damaged, mildly damaged, and least damaged particles, respectively. g) The relative population of these three kinds of particles, which changes as a function of the cycling history, is summarized in the radar chart.

and show excellent image contrast (black; see red arrows in Figure 1i); while other cracks are less visible (gray; see green arrows in Figure 1i). The less visible cracks are likely in the early stage of the crack development. The reduced visibility is due to a significant amount of subpixel-level porosity corresponding to the fine microcracks, which are often beyond the spatial resolution limit of the X-ray spectromicroscopy (at  $\approx 30$  nm).

The Ni redox couple is a major charge compensation mechanism for lithium intercalation/deintercalation in nickel-rich NMCs. As a result, the Ni K-edge absorption energy is often used as a proxy for the local SoC. The surface of the particle and the well-developed cracks appear to be more oxidized in Figure 1j as indicated by the red contour. The well-developed cracks facilitate the infiltration of the liquid electrolyte, activating the lithium-ion deintercalation at the crack surface. In contrast, the change in the spectroscopic fingerprint over the newly developed cracks is less obvious. We extract the cracks with weaker visibility based on the grayscales in Figure 1i and segment the Ni valence map accordingly. As shown in Figure 1k, the newly developed cracks are scattered throughout the particle. There is not an obvious contrast (in terms of the Ni oxidation state) between the bulk and the cracks at their early stage of development. This is likely due to the lack of liquid electrolyte wetting at these regions.

### 2.1.3. The Cathode Particle's Structural Degradation at the Electrode Level upon Prolonged Fast Cycling

The mesoscale structural and chemical complexity can be further amplified at the electrode level. In a real-life battery

cathode electrode, secondary particles are embedded in the porous matrix of carbon additives and binder. Close packing of active materials is essential to ensure the desired volumetric energy density. In addition to accommodating the active particles, the porous carbon matrix is also responsible for providing the electrical contact throughout the electrode. The liquid electrolyte soaks the porous matrix and provides an interconnected diffusion network for the lithium ions. The mismatch in the local electrical and ionic conductivity, both of which could change as a function of time and position, can lead to reaction heterogeneity at the electrode scale, which is closely relevant to the real-life cell aging and ultimate failure.

We show in Figure 2 the results of X-ray phase contrast tomography of the electrochemically cycled NMC622 electrode (10 cycles from 2.5 to 4.5 V with a rate of 5C). For penetrating the thick electrode, the X-ray imaging was carried out at a high energy (17 keV), which, unfortunately, sacrificed the absorption contrast and, thus, accentuated the need for the sensitivity improvement through phase contrast methodology.<sup>[38,39]</sup> Figure 2a is an overview of the electrode (phase contrast microtomography data, 650 nm pixel size), with a magnified ROI (70 nm pixel size) shown in Figure 2b and a selected slice through the center of the ROI shown in Figure 2c. Three of the representative particles are highlighted in red (Figure 2d, severely damaged), green (Figure 2e, mildly damaged), and blue (Figure 2f, least damaged). Further comparison of the quantification results of the electrodes with different cycling history (10 cycles vs 50 cycles, with same lower/upper cutoff voltages and cycling rate) is shown in Figure 2g, suggesting that the particle cracking continues to develop upon electrochemical cycling.

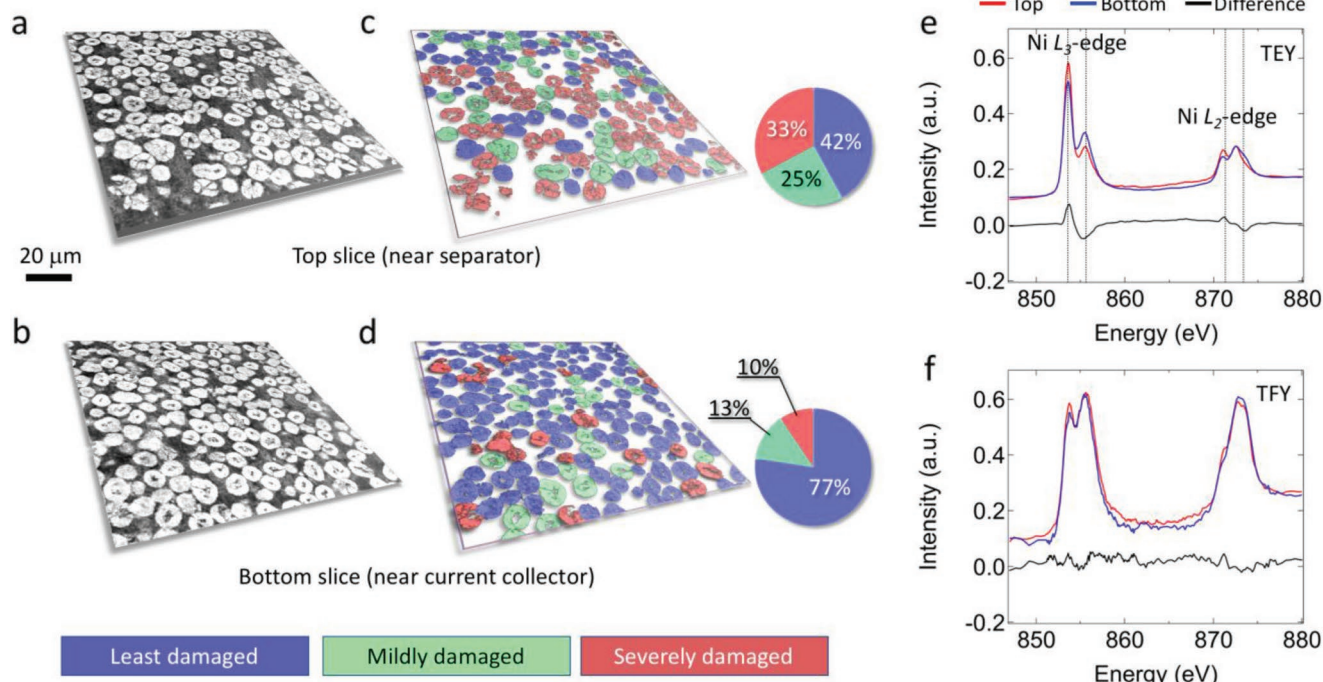


**Figure 3.** The comparison of the top and the bottom layers in the NMC622 electrode that has gone through 10 fast cycles at a rate of 5C. a,c) (Color-coded) The same lateral slice over the particle layer that is close to the ten-cycled electrode's top surface (near the separator). b,d) (Color-coded) The same lateral slices over the first layer of particles close to the aluminum current collector (bottom of the ten-cycled electrode). The relative particle cracking probabilities over these two slices are quantified in the corresponding pie charts. e,f) The surface-sensitive soft XAS results over the top (red) and the bottom (blue) of the ten-cycled electrode in TEY and TFY modes, respectively.

## 2.2. The Position-Dependent Degradation Profile at the Electrode Scale

The X-ray phase contrast nanotomography data cover over a thousand active particles with a pixel size down to  $\approx 70$  nm. Such unprecedented amount of morphological details facilitates a more detailed quantification. We show in **Figure 3a–d** two lateral virtual slices ( $xy$  plane) at different  $z$  positions from the 40- $\mu\text{m}$ -thick electrode. Figure 3a represents the slice near the top surface of the electrode ( $\approx 5$   $\mu\text{m}$  from the top surface, close to separator), while Figure 3b is the data near bottom surface ( $\approx 5$   $\mu\text{m}$  from the bottom surface, near the aluminum current collector). Figure 3c,d are the same slices color-coded based on the severity of particle fracturing. The corresponding relative probability distribution is shown in the insets next to Figure 3c,d, respectively. It is evident in our observation that a distinguished pattern of a depth-dependent particle fracturing has developed in the electrode upon fast cycling.

To understand the chemical implications of the different degree of structural degradation at the top and the bottom of the electrode, we carried out surface-sensitive soft XAS measurements over the top and bottom of the electrode. The total electron yield (TEY, probing depth at  $\approx 10$  nm) and total fluorescence yield (TFY, probing depth at  $\approx 100$  nm) signals are acquired over the absorption L-edges of Ni (Figure 3e,f), Mn, Co, and the K-edge of O (Figure S1, Supporting Information), respectively. In nickel-rich NMC cathode, Ni's redox reaction is the major mechanism for the charge compensation during repeated lithium (de)intercalation. We, therefore, present the

Ni L-edge data in Figure 3e,f for in-depth discussions. In the TEY mode, Ni<sup>2+</sup> component is clearly observed on both the top and bottom layers (Figure 3e), suggesting a notable surface reconstruction<sup>[40]</sup> that happens throughout the entire electrode under fast charging conditions. We point out here that the TEY probing depth is up to  $\approx 10$  nm, which is significantly smaller than the spatial resolution limit of the X-ray spectromicroscopy. Therefore, the thin surface layer with transformed lattice structure is not visible in Figure 1j. The difference shown in Figure 3e indicates that the top of the electrode experienced more severe undesired local phase transition from the layered structure to a mixture of spinel and rock salt structure.<sup>[40]</sup> In contrast, the TFY signal, which probes deeper into the bulk, shows negligible difference between the top and bottom of the electrode. This observation suggests that, at the electrode level, there is not a significant SoC heterogeneity between the top and the bottom of the electrode after long-term relaxation. While the mesoscale SoC heterogeneity within individual secondary particles could persist after long-term relaxation,<sup>[41]</sup> it does not seem to be the case at the electrode level as the charge transfer among the active particles could be facilitated by the well-interconnected liquid electrolyte and conductive carbon networks.<sup>[42]</sup>

The cracking patterns' depth profiles over representative regions of a 10-cycled and a 50-cycled electrodes are summarized in Tables S1 and S2 (Supporting Information), with the plots shown in **Figure 4a**. The ten-cycled electrode demonstrates a clear depth dependence in its fracturing profile, in a good agreement with the soft XAS data shown in Figure 3e

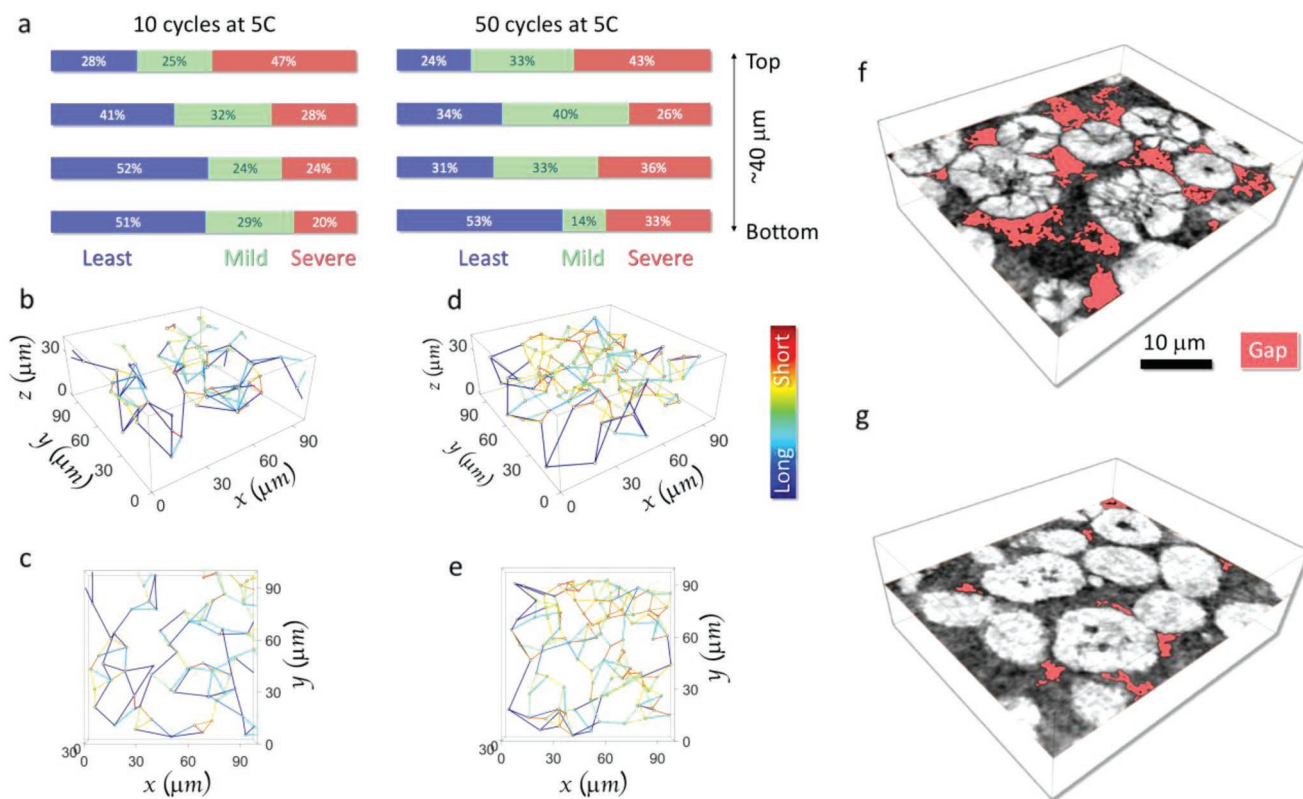


**Figure 4.** The comparison of the fracturing profiles in the fast-cycled (5C) electrodes for 10 cycles and 50 cycles. a) The fracturing profiles across the top to the bottom of the electrodes, of which the ten-cycled electrode (left) shows a clear depth dependency. b) (10-cycled electrode) and d) (50-cycled electrode) are the 3D representation of the severely fractured particle network, c,e) with the corresponding top views, respectively. f,g) Two selected local regions with different degrees of particle fracturing (near the top and bottom of the ten-cycled electrode, respectively; also see Figure S4, Supporting Information, for the raw data without labels). The detachment of the active particles from the conductive carbon network correlates positively with the degree of fracturing. The void volume near the particle surface is labeled as gap in panels (f) and (g).

as the particle fracturing would expose more crack surface, which will experience the lattice reconstruction forming divalent Ni.<sup>[40]</sup> The 50-cycled electrode, on the other hand, shows more severe morphological damage and, thus, breaks down the depth dependence. Generally speaking, the degree of particle fracturing is positively correlated with the degree of active material utilization. Our data in Figure 4a suggest that the active materials at different depth contribute to the cell level chemistry differently in both time and position. In the early cycles, particles near the separator account for more of the charge compensation, possibly, due to their favorable lithium diffusion rates. The higher degree of reaction near the separator causes more severe local degradation, which could partially deactivate the particles in this region by detaching the particles from the conductive carbon network (see Figure 4f,g). We highlight here that the separation of active, inactive, and pore phase at nanoscale is reliable in our study thanks to the excellent sensitivity offered by the X-ray phase contrast methodology. Similar dynamic particle detachment/damage effects are also observed in conversion type of Si anode electrode.<sup>[24,43]</sup> Subsequently, the particles that are located deeper in the electrode take over the electrochemical activities in the later cycles, making the depth-dependent fracturing profile less apparent as suggested by Figure 4a.

In addition to the depth-dependent fracturing profile, which is a 1D representation of the inhomogeneous degree of active material utilization at the electrode level, our imaging data also offer valuable insights into the lateral and, more importantly, the 3D complexity. Indeed, the lateral SoC heterogeneity at the electrode level has been reported and appreciated as a consequence of the electrode aging.<sup>[31]</sup> With the extraction of the 3D centroid coordinates of all the severely damaged particles, here we develop a method to construct a network that connects all these particles based on their spatial distribution. For every severely damaged particle, our method searches for three of its nearest neighbors of the same kind and uses color-coded bounds to connect them (see Figure 4b–e and the corresponding color map in the inset of Figure 4d). As the degree of particle cracking is positively correlated to the degree of active particle usage, we conjecture that the extracted network scales with the 3D distribution of the local current density. The perspective and the top views of the networks for 10-cycled and 50-cycled electrodes are shown in Figure 4b,c and 4d,e, respectively. After the first 10 cycles, the heavily used particles are sparsely scattered throughout the 3D volume of the electrode. This is likely due to their favorable and balanced electrical and ionic conductivity. After 50 cycles, this network becomes denser because of the activation of more particles upon prolonged

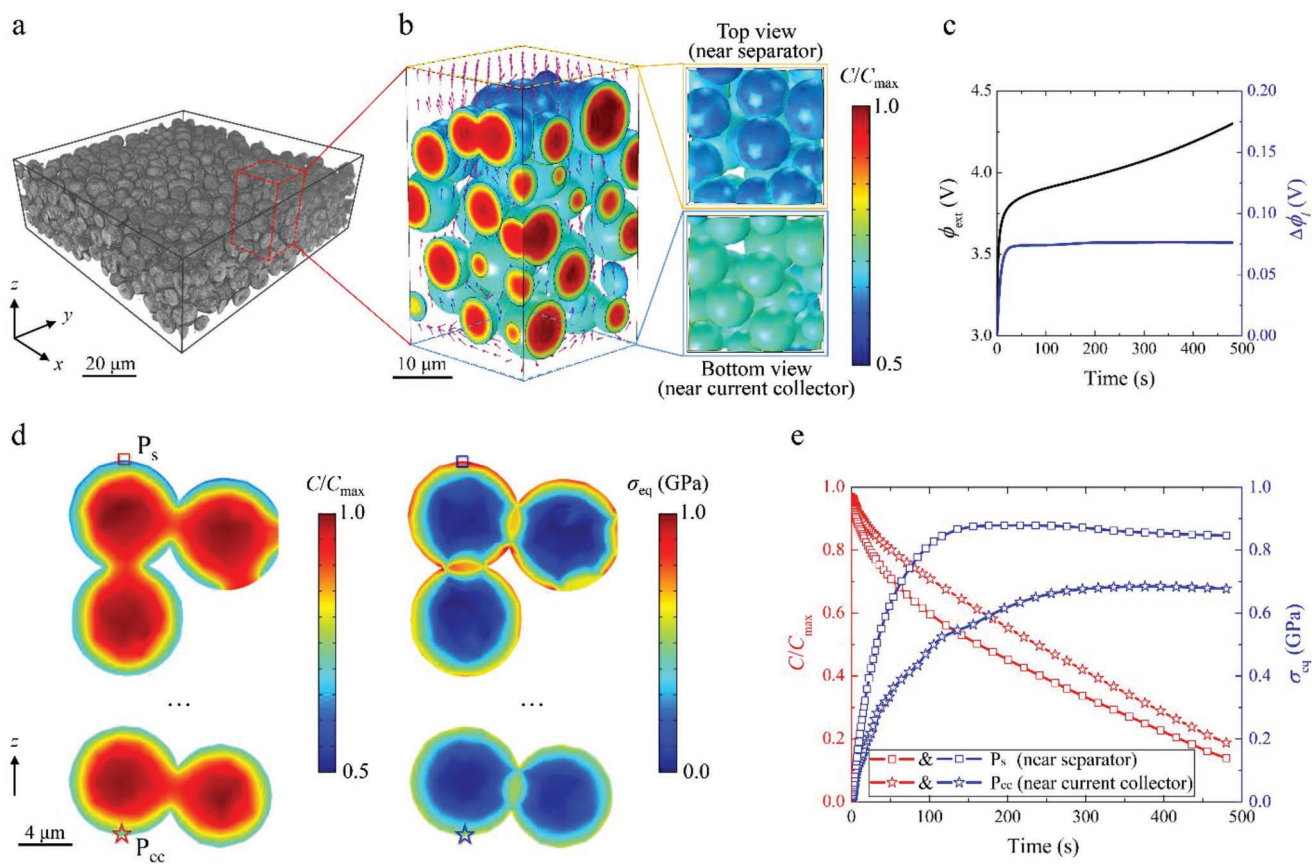


**Figure 5.** Finite element analysis of the heterogeneous electrochemistry and mechanics in a NMC composite electrode. a) A 3D rendering of the nanotomography data of an arbitrarily selected region ( $120\ \mu\text{m} \times 120\ \mu\text{m} \times 40\ \mu\text{m}$ ) in the NMC622 cathode. Geometrical data extracted from 1/36 of the region (marked by a red box,  $20\ \mu\text{m} \times 20\ \mu\text{m} \times 40\ \mu\text{m}$ ) are used to generate a representative volume element for the theoretical modeling. b) The normalized Li concentration within the NMC particles and the local Li flux (arrows) within the electrolyte in the composite electrode. The SoC in the particles near the separator (top) is higher than those near the current collector (bottom). c) Plots of the external voltage  $\phi_{\text{ext}}$  and electrolyte voltage drop  $\Delta\phi_i$  of the half-cell charged at the 5C rate. The electrolyte voltage drop along the depth direction in the electrode causes the different SoC in panel (b). d) The cross-sectional view of Li concentration (left) and the internal stress  $\sigma_{\text{eq}}$  (right) in the NMC particles near the separator (upper) versus near the current collector (lower). The particles near the separator experience a larger Li flow and, thus, larger stresses, which promote crack formation and particle disintegration. e) The time evolution of Li concentration and equivalent stress at two locations,  $P_s$  (near separator) and  $P_{cc}$  (near current collector), are plotted.

battery operation. The particle-to-particle distance clearly becomes smaller as it can be seen in the topological representations in Figure 4d,e.

### 2.3. Finite Element Modeling of the Electrode Degradation Mechanism

We further performed finite element analysis to understand the depth heterogeneous electrochemistry and mechanics of the NMC composite electrode. The 3D nanotomography data of an arbitrarily selected region ( $120\ \mu\text{m} \times 120\ \mu\text{m} \times 40\ \mu\text{m}$ , Figure 5a) in NMC electrode are utilized to reconstruct a representative volume element (RVE) ( $20\ \mu\text{m} \times 20\ \mu\text{m} \times 40\ \mu\text{m}$ ). The RVE is integrated into a half-cell configuration that is under galvanostatic charging (delithiation). The fields of electrical potential, Li concentration, and mechanical stresses in NMC are simultaneously solved. Figure 5b shows the distribution of Li concentration  $C/C_{\text{max}}$  within NMC particles and local Li flux

(arrows) within the electrolyte at the charging time  $t = 150\ \text{s}$ . It shows that the NMC particles near the separator (top) experience a higher SoC than those near the current collector (bottom). Top and bottom views in the right panel of Figure 5b also confirm the different delithiation states. The highly delithiated surface of NMC particles near the separator would induce a more severe phase transition from the layered structure to a mixture of the spinel and rock salt structures, which is consistent with the surface sensitive soft XAS TEY results in Figure 3e.

The depth heterogeneity in the NMC electrode is due to the inhomogeneous electrochemical driving force for the charge transfer at the interface between the NMC particles and the electrolyte. Figure 5c plots the external voltage  $\phi_{\text{ext}}$  and the electrolyte voltage drop  $\Delta\phi_i$  as a function of the charging time. The external voltage  $\phi_{\text{ext}}$  is measured as the electric potential at the cathode current collector, by assuming that the Li metal anode has an electric potential of 0 V. Since the electrical conductivity of carbon-binder matrix is high, the electric potential in

carbon-binder matrix  $\phi_c$  is homogeneous throughout the entire NMC cathode (same as  $\phi_{\text{ext}}$ ). However, the electric potential  $\phi_l$  caused by diffusion and migration of charged species in the liquid electrolyte is inhomogeneous, forming a nearly constant positive electrolyte voltage drop  $\Delta\phi_l$  (i.e.,  $\phi_l$  at the cathode current collector minus  $\phi_l$  at the separator). As a result, the effective electric potential ( $\phi_c - \phi_l$ ) acting on the NMC particle outer surface near the separator is higher, as shown in Figure S5a (Supporting Information). The activation overpotential  $\eta$  for charge transfer at the particles/electrolyte interface is defined as  $\eta = (\phi_c - \phi_l) - E_{\text{eq}}$ , where  $E_{\text{eq}}$  is the equilibrium potential for the Li reaction in NMC and is solely dependent on the SoC (Figure S5a, Supporting Information). Therefore, the overpotential  $\eta$  cross the particle/electrolyte interface near the separator is higher than that near current collector (Figure S5b, Supporting Information) and the NMC particles near the separator experience a higher electron transfer density as well as a larger Li outflux (Figure S5c, Supporting Information).

Next, we investigate the electrochemical and mechanical variables at the particle scale. Figure 5d shows the cross-sectional view of Li concentration  $C/C_{\text{max}}$  (left panel) and the equivalent stress  $\sigma_{\text{eq}}$  (right panel) in the NMC particles near the separator (upper panel) versus near the current collector (lower panel) at the charging time  $t = 150$  s. At the fast charging condition, Li near the surface of NMC particles is quickly depleted while Li near the core of NMC maintains a relatively high concentration. Because the NMC particles near the separator undergo a higher Li flux, they are subject to larger diffusion-induced stresses (upper right panel in Figure 5d). These stresses further promote crack formation and thus particle disintegration near the separator, as supported by Figure 3a–d. For a quantitative comparison, we plot the time evolution of Li concentration and equivalent stresses at two specific locations,  $P_s$  (near separator) and  $P_{\text{cc}}$  (near current collector) in Figure 5e. The result demonstrates that the differences in Li concentration and stress in the two locations remain about the same during the entire charging process, which induce more particle damages near the separator.

### 3. Conclusion

It is generally appreciated that the electro-chemo-mechanical processes in lithium-ion batteries are ubiquitous across a wide range of length scales. While the transformation in the lattice structure at the atomic scale is often regarded as the root causes of a range of degradation phenomena the complexity is further amplified at the mesoscale (within the secondary particles) and the macroscale (at the electrode level). To truly understand the intertwined, heterogeneous, and hierarchical electro-chemo-mechanical coupling effects in composite battery electrodes, imaging techniques that can resolve features at different length scales have to be combined. More specifically, it is desirable to conduct electrode scale imaging with nanometric resolution. Such dataset could offer unprecedented amount of structural information, which would facilitate sophisticated and valuable statistical analysis.

In this work, we started at the atomic scale and used TEM to visualize the coexisting layered and rock salt lattice structures

over a cracked area. The local lattice deformation can serve as nucleation points for further development of the structural defects. Coupled with nanoscale X-ray spectromicroscopy and transmission X-ray microscopy, we then reconstructed the mesoscale morphological and chemical transformations in the NMC622 secondary particles under fast charging conditions. We quantified the particle morphology as well as the local SoC distribution and, subsequently, elucidated the mesoscale chemo-mechanical degradation mechanism that involves (1) the host material's local lattice structural transition and (2) liquid electrolyte infiltration that forms new diffusion pathway for lithium ions. Furthermore, we conducted hard X-ray phase contrast nanotomography of the cathode electrode with nanometric spatial resolution. We extracted the complicated structural degradation profile across the cathode electrode and presented the depth-dependent trend of particle fracturing as well as its lateral complexity. We developed a method to reconstruct the 3D topological representation of the local current density distribution. Our results suggest that the active particles within the electrode contribute to the cell level chemistry differently in time and position. The degradation depth profile shows initially more damage near the separator, evolving to a more homogeneous distribution as particles located deeper in the electrode take over the electrochemical activities in later cycles. Finally, FEM was used to model the spatial and temporal evolution of the Li concentration and mechanical stresses in the electrode, offering further in-depth understanding of the fundamental mechanism behind the observed heterogeneous structural damage at the electrode level. The presented findings and their implications offer insights into designing chemo-mechanically robust battery particles and formulating fast charge capable electrodes.

### 4. Experimental Section

**Transmission Electron Microscopy:** The TEM study was performed using a JOEL-2100 S/TEM microscope operated at 200 kV. The FFT and IFFT images were carried out using Gatan Digital Micrograph software.

**Nanoresolution X-Ray Spectromicroscopy:** X-ray spectromicroscopic scan of the charged  $\text{Li}_{0.5}\text{Ni}_{0.6}\text{Mn}_{0.2}\text{Co}_{0.2}\text{O}_2$  particles was conducted using the transmission X-ray microscopy (TXM) at beamline 6-2C of Stanford Synchrotron Radiation Lightsource (SSRL) of the SLAC National Accelerator Laboratory. The powder sample was loaded into a quartz capillary (100  $\mu\text{m}$  in diameter and 10  $\mu\text{m}$  in wall thickness) for imaging under the inert gas environment (slow and steady helium flow). The typical exposure time for single images is 0.5 s. The nominal spatial resolution of this instrument is  $\approx 30$  nm. More details of the synchrotron beamline configuration and the concept of X-ray spectromicroscopy and spectrotomography can be found elsewhere.<sup>[36,44]</sup> In the 3D spectromicroscopic scan, the energy of the incident X-rays is scanned from 8200 to 8630 eV to cover the absorption K-edges of Ni, in which the tomography was performed at 68 different energy points. In the near edge region (8330–8355 eV), the energy step at 1 eV was chosen to ensure sufficient energy resolution. The pre-edge and post-edge regions were scanned with larger energy steps of 10 eV to cover a relatively wide energy window for normalization of the spectra. The TXM data processing was performed using an in-house developed software package known as TXM-Wizard.<sup>[45]</sup> The segmentation and visualization of the 3D data were carried out using a commercial software package known as Avizo.

**Soft X-Ray Absorption Spectroscopy:** The soft XAS measurements were carried out at the elliptically polarizing undulator (EPU) beamline 13-3 of the SSRL. The charged NMC622 electrodes were mounted

in an ultrahigh vacuum (UHV) chamber for the measurement. For comparison of the top and bottom of the electrode, the aluminum current collector was carefully peeled off and two pieces of the electrode were mounted facing up and down, respectively. The samples were handled in an argon-filled glove box to minimize the air exposure. The vertically polarized X-ray (sigma-polarization) was used. The incident beam was monochromatized by a 1100 lines  $\text{mm}^{-1}$  spherical grating monochromator (SGM), and its angle was set at  $30^\circ$  from the sample surface. Both fluorescence yield (FY) and TEY signals were acquired simultaneously to probe the depth-dependent spectroscopic fingerprints. All the XAS spectra were normalized by the intensity of the incoming X-ray beam that was concurrently measured as a drain current on an electrically isolated gold-coated mesh. A linear background, which was determined by the intensity of the pre-edge region, was subtracted from the data.

**X-Ray Phase Contrast Nanotomography:** For the morphological study of the microscale structures of the Li battery cathode, synchrotron hard X-ray nanotomography based on phase contrast with high spatial resolution becomes the method of choice. The so-called holotomography measurements of the samples were conducted at the ID16A-NI nanoimaging beamline<sup>[46]</sup> of the European Synchrotron Radiation Facility (ESRF) in Grenoble, France. This beamline offers a unique combination of nanofocus ( $\approx 20$  nm) and a very high photon flux (up to  $10^{12}$  photons  $\text{s}^{-1}$  at  $\Delta E/E \approx 1\%$ ). Two pairs of multilayer coated Kirkpatrick-Baez (KB) optics were used to focus the X-rays at 17 and 33.6 keV, respectively. This experiment was performed at 17 keV. Besides the benefits of the ability to perform nanotomography with a high energy, the magnifying geometry of the cone beam also allows large field of view (FOV) with 100 and 70 nm voxel size. Due to free space propagation of the X-ray beam, the contrast in the images is dominated by phase contrast, related to the real part of the complex refractive index, which is determined by the electron density of the material. By measuring the Fresnel diffraction patterns at different effective propagation distances, the phase maps of the sample can be retrieved via holographic reconstruction, the so-called phase retrieval procedure<sup>[47]</sup> implemented using GNU Octave software. In the measurements, the sample was placed downstream of the KB focus and magnified radiographs were recorded onto an X-ray detector using a FReLoN charged-coupled device (CCD) with a  $2048 \times 2048$  binned pixels array. For every tomography scan, 1500 projections were acquired with 0.2 s exposure time. Tomographies at four different focus-to-sample distances were acquired to complete one holotomography scan, which were subsequently used for phase retrieval. The 2D phase maps retrieved from the angular projections were then used as input for a tomographic reconstruction based on the filtered back projection (FBP) algorithm method (ESRF PyHST software package).<sup>[48]</sup> The reconstructed 3D volumes are proportional to the changes in electron density of the sample.

**Particle Edge Detection, Segmentation, and Labeling:** The single-voxel-thick slices shown in Figure 3a–d cut through the particles at different depth due to the random arrangement of the particles in the electrode. For a more precise quantification of the cracking profile, here a more advanced approach was developed. As a first step, mild median filtering was applied to the 3D image for improving the signal-to-noise ratio before conducting the particle edge detection (Figure S2, Supporting Information) based on Canny edge detection algorithm<sup>[49]</sup> using the FeatureJ plugin<sup>[50]</sup> in ImageJ<sup>[51]</sup> software. The image filtering trades the image resolution, which is less important for the purpose of automatic particle detection and segmentation, for the reduction of the noise. The detected particle boundary was then used to automatically isolate individual particles from the 3D representation of the whole electrode. The 3D volume was summed in any given  $10\text{-}\mu\text{m}$ -thick depth window in the Z-direction. The projected image (Figure S2, Supporting Information) was then used for identification and labeling of particles based on their degree of fracturing (Figure S3, Supporting Information). This procedure was repeated for the data subvolume in different Z windows.

**Finite Element Modeling:** 3D NMC composite models were reconstructed based on the nanotomography data of an arbitrarily selected region ( $120\ \mu\text{m} \times 120\ \mu\text{m} \times 40\ \mu\text{m}$ ) in NMC cathode.

Geometrical data including the coordinate of the particle centers and equivalent particle radii were extracted from 1/36 of the selected region ( $20\ \mu\text{m} \times 20\ \mu\text{m} \times 40\ \mu\text{m}$ ). Since the majority of the NMC particles are spherical in nature, a RVE that contains 52 spherical particles was built.<sup>[52]</sup> The empty space of RVE was filled with the electrolyte and carbon-binder matrix (not explicitly modeled). The volume fractions of NMC particles and electrolyte in the composite electrode were 41 and 30%, respectively. Only the electron transfer was considered for the conductive matrix because the conductive matrix was impermeable for Li ions. The electrolyte only transported Li ions and the active material conducted both Li ions and electrons (Figure S6a, Supporting Information). The reconstructed NMC electrode was then integrated into a half-cell configuration (Figure S6b, Supporting Information). Since the electronic conductivity of Li metal was high, the thickness of the Li metal anode had negligible impact on the cell voltage and polarization. A finite element program based on an electro-chemo-mechanical coupled theory using the commercial software COMSOL Multiphysics was developed. This finite element program was utilized to simultaneously solve the electrochemistry and mechanics fields in the half-cell. To simulate the galvanostatic charging, the cathode current collector side was applied a constant current and its magnitude was determined based on the specific charging rate. A refined mesh was used for the numerical model to improve the accuracy (Figure S6c, Supporting Information).

**Details About the Sample Preparation:** The composite cathodes were prepared by spreading the slurry (N-methyl-2-pyrrolidone as the solvent) with active materials (90 wt%), acetylene carbon (5 wt%), and polyvinylidene fluoride (PVdF) (5 wt%) as the binder and casting them on carbon-coated aluminum foils. The electrodes were then dried overnight at  $120^\circ\text{C}$  in a vacuum oven and transferred into an Ar-filled glove box for future use. The areal active mass loading is  $\approx 8.0\ \text{mg cm}^{-2}$ . The volume fractions of active particles, the liquid electrolyte, and the carbon-binder matrix are about 40, 30, and 30%, respectively. It resulted in the porosity of the homogenized matrix being 0.5. This relatively high porosity is because the electrode was not calendared in order to avoid any predamaged caused by the calendaring process. It is noted that there is a small depth-dependent variation of the particle concentration in the electrode (see Figure S7, Supporting Information). For the ex situ measurements, the electrodes were charged to the designated state of charge (capacity) or cycle number, and then the cells were disassembled in an Ar-filled glove box. It is shown the voltage–capacity curves at the 1st, 10th, and 50th cycle in Figure S8 (Supporting Information), which suggests that the cell underwent gradual capacity fading and the cell overpotential increased as the cycle number increased. For the TEM measurements, the electrode particles were scratched off the electrode and deposited onto TEM grids. For the nanoresolution X-ray spectromicroscopy measurements, the electrode particles were scratched off the electrode and loaded into quartz capillary tubes ( $100\ \mu\text{m}$  in diameter and  $10\ \mu\text{m}$  in wall thickness). For the soft XAS measurement, all battery electrode samples were attached to an aluminum sample holder using conductive carbon tapes, which is necessary for the detection of TEY signal. For the soft XAS measurements on the current collector side, the electrodes were peeled from the current collector and the electrolyte side was attached to the conductive carbon tapes. The charged or cycled electrodes were directly used for the X-ray phase contrast nanotomography. For X-ray phase contrast nanotomography, the sample was a small piece cut carefully from a complete cathode plate, then fixed on top of a Huber pin in order to mount in the rotation stage. The tomography scan was about the center of the piece, away from the cut edges to avoid any sample prep induced artifacts. All the samples were protected in the inert gas environment during storage, transportation, handling, and measurements.

## Supporting Information

Supporting Information is available from the Wiley Online Library or from the author.

## Acknowledgements

Y.Y., R.X., K.Z. (Kai Zhang), and S.-J.L. contributed equally to this work. Use of the Stanford Synchrotron Radiation Lightsource, SLAC National Accelerator Laboratory, was supported by the U.S. Department of Energy, Office of Science, Office of Basic Energy Sciences under Contract No. DE-AC02-76SF00515. Part of this work was performed at the Stanford Nano Shared Facilities (SNSF), supported by the National Science Foundation under Award No. ECCS-1542152. The hard X-ray phase contrast tomography was conducted at the Nano-Imaging beamline ID16A-NI at the ESRF, Grenoble, France. F.L. and K.Z. (Kejie Zhao) acknowledge support from the National Science Foundation under Grant Nos. DMR-1832613 and DMR-1832707, respectively. The NMC electrodes were produced at the U.S. Department of Energy's (DOE) CAMP (Cell Analysis, Modeling and Prototyping) Facility, Argonne National Laboratory. The CAMP Facility was fully supported by the DOE Vehicle Technologies Program (VTP) within the core funding of the Applied Battery Research (ABR) for Transportation Program. The work performed at Institute of High Energy Physics was partly supported by the National Key Research and Development Program of China (Grant No. 2016YFA0400900) and the National Natural Science Foundation of China (Grant Nos. 11535015 and U1632110). The engineering support from D. Van Campen, D. Day, and V. Borzenets for the TXM experiment at beamline 6-2C of SSRL is gratefully acknowledged.

## Conflict of Interest

The authors declare no conflict of interest.

## Keywords

chemomechanical interplay, fast charging, finite elemental modeling, NMC cathode, structural degradation, X-ray phase contrast tomography

Received: February 26, 2019

Revised: April 25, 2019

Published online: May 28, 2019

- [1] S.-M. Bak, Z. Shadik, R. Lin, X. Yu, X.-Q. Yang, *NPG Asia Mater.* **2018**, *10*, 563.
- [2] W. Liu, P. Oh, X. Liu, M. J. Lee, W. Cho, S. Chae, Y. Kim, J. Cho, *Angew. Chem., Int. Ed.* **2015**, *54*, 4440.
- [3] H. Lu, H. Zhou, A. M. Svensson, A. Fossdal, E. Sheridan, S. Lu, F. Vullum-Bruer, *Solid State Ionics* **2013**, *249*, 105.
- [4] M.-H. Kim, H.-S. Shin, D. Shin, Y.-K. Sun, *J. Power Sources* **2006**, *159*, 1328.
- [5] H.-H. Ryu, K.-J. Park, C. S. Yoon, Y.-K. Sun, *Chem. Mater.* **2018**, *30*, 1155.
- [6] F. Yang, Y. Liu, S. K. Martha, Z. Wu, J. C. Andrews, G. E. Ice, P. Pianetta, J. Nanda, *Nano Lett.* **2014**, *14*, 4334.
- [7] J. Xu, F. Lin, M. M. Doeff, W. Tong, *J. Mater. Chem. A* **2017**, *5*, 874.
- [8] M. Guilmard, L. Croguennec, C. Delmas, *Chem. Mater.* **2003**, *15*, 4484.
- [9] I. Saadoune, C. Delmas, *J. Mater. Chem.* **1996**, *6*, 193.
- [10] E. Zhecheva, R. Stoyanova, *Solid State Ionics* **1993**, *66*, 143.
- [11] Z. Xu, M. M. Rahman, L. Mu, Y. Liu, F. Lin, *J. Mater. Chem. A* **2018**, *6*, 21859.
- [12] S. Xia, L. Mu, Z. Xu, J. Wang, C. Wei, L. Liu, P. Pianetta, K. Zhao, X. Yu, F. Lin, Y. Liu, *Nano Energy* **2018**, *53*, 753.
- [13] R. Xu, L. S. de Vasconcelos, J. Shi, J. Li, K. Zhao, *Exp. Mech.* **2018**, *58*, 549.
- [14] P. Yan, J. Zheng, M. Gu, J. Xiao, J. G. Zhang, C. M. Wang, *Nat. Commun.* **2017**, *8*, 14101.
- [15] L. Mu, R. Lin, R. Xu, L. Han, S. Xia, D. Sokaras, J. D. Steiner, T. C. Weng, D. Nordlund, M. M. Doeff, Y. Liu, *Nano Lett.* **2018**, *18*, 3241.
- [16] L. Mu, Q. Yuan, C. Tian, C. Wei, K. Zhang, J. Liu, P. Pianetta, M. M. Doeff, Y. Liu, F. Lin, *Nat. Commun.* **2018**, *9*, 2810.
- [17] P. Yan, J. Zheng, T. Chen, L. Luo, Y. Jiang, K. Wang, M. Sui, J. G. Zhang, S. Zhang, C. Wang, *Nat. Commun.* **2018**, *9*, 2437.
- [18] C. Wei, Y. Zhang, S.-J. Lee, L. Mu, J. Liu, C. Wang, Y. Yang, M. Doeff, P. Pianetta, D. Nordlund, *J. Mater. Chem. A* **2018**, *6*, 23055.
- [19] D. P. Finegan, M. Scheel, J. B. Robinson, B. Tjaden, I. Hunt, T. J. Mason, J. Millichamp, M. Di Michiel, G. J. Offer, G. Hinds, *Nat. Commun.* **2015**, *6*, 6924.
- [20] F. Lin, Y. Liu, X. Yu, L. Cheng, A. Singer, O. G. Shpyrko, H. L. Xin, N. Tamura, C. Tian, T.-C. Weng, X.-Q. Yang, *Chem. Rev.* **2017**, *117*, 13123.
- [21] J. Wang, Y.-C. K. Chen-Wiegart, C. Eng, Q. Shen, J. Wang, *Nat. Commun.* **2016**, *7*, 12372.
- [22] Z. Zhang, Q. Zhang, J. Shi, Y. S. Chu, X. Yu, K. Xu, M. Ge, H. Yan, W. Li, L. Gu, Y. S. Hu, *Adv. Energy Mater.* **2017**, *7*, 1601196.
- [23] M. Ebner, F. Marone, M. Stamparoni, V. Wood, *Science* **2013**, *342*, 716.
- [24] S. Müller, P. Pietsch, B.-E. Brandt, P. Baade, V. De Andrade, F. De Carlo, V. Wood, *Nat. Commun.* **2018**, *9*, 2340.
- [25] P.-C. Tsai, B. Wen, M. Wolfman, M.-J. Choe, M. S. Pan, L. Su, K. Thornton, J. Cabana, Y.-M. Chiang, *Energy Environ. Sci.* **2018**, *11*, 860.
- [26] C. Wei, S. Xia, H. Huang, Y. Mao, P. Pianetta, Y. Liu, *Acc. Chem. Res.* **2018**, *51*, 2484.
- [27] N. Besnard, A. Etienne, T. Douillard, O. Dubrunfaut, P. Tran-Van, L. Gautier, S. Franger, J.-C. Badot, E. Maire, B. Lestriez, *Adv. Energy Mater.* **2017**, *7*, 1602239.
- [28] J. Wang, J. Wu, Z. Wu, L. Han, T. Huang, H. L. Xin, D. Wang, *Electrochim. Acta* **2017**, *244*, 8.
- [29] S. Kuppan, Y. Xu, Y. Liu, G. Chen, *Nat. Commun.* **2017**, *8*, 14309.
- [30] C. R. Becker, K. E. Strawhecker, Q. P. McAllister, C. A. Lundgren, *ACS Nano* **2013**, *7*, 9173.
- [31] J. Nanda, J. Remillard, A. O'Neill, D. Bernardi, T. Ro, K. E. Nietering, J. Y. Go, T. J. Miller, *Adv. Funct. Mater.* **2011**, *21*, 3282.
- [32] Y. Liu, A. M. Kiss, D. H. Larsson, F. Yang, P. Pianetta, *Spectrochim. Acta, Part B* **2016**, *117*, 29.
- [33] X. Duan, F. Yang, E. Antono, W. Yang, P. Pianetta, S. Ermon, A. Mehta, Y. Liu, *Sci. Rep.* **2016**, *6*, 34406.
- [34] K. Zhang, F. Ren, X. Wang, E. Hu, Y. Xu, X.-Q. Yang, H. Li, L. Chen, P. Pianetta, A. Mehta, X. Yu, *Nano Lett.* **2017**, *17*, 7782.
- [35] W. H. Kan, B. Deng, Y. Xu, A. K. Shukla, T. Bo, S. Zhang, J. Liu, P. Pianetta, B.-T. Wang, Y. Liu, G. Chen, *Chem* **2018**, *4*, 2108.
- [36] F. Meirer, J. Cabana, Y. Liu, A. Mehta, J. C. Andrews, P. Pianetta, *J. Synchrotron Radiat.* **2011**, *18*, 773.
- [37] C. Tian, Y. Xu, D. Nordlund, F. Lin, J. Liu, Z. Sun, Y. Liu, M. M. Doeff, *Joule* **2018**, *2*, 464.
- [38] M. Hubert, J. Laurencin, P. Cloetens, B. Morel, D. Montinaro, F. Lefebvre-Joud, *J. Power Sources* **2018**, *397*, 240.
- [39] H. Fang, C. Versteyle, S. Zhang, Y. Yang, P. Cloetens, D. Ngan-Tillard, E. Brück, S. van der Zwaag, N. van Dijk, *Acta Mater.* **2016**, *121*, 352.
- [40] F. Lin, I. M. Markus, D. Nordlund, T.-C. Weng, M. D. Asta, H. L. Xin, M. M. Doeff, *Nat. Commun.* **2014**, *5*, 3529.
- [41] W. E. Gent, Y. Li, S. Ahn, J. Lim, Y. Liu, A. M. Wise, C. B. Gopal, D. N. Mueller, R. Davis, J. N. Weker, J. H. Park, *Adv. Mater.* **2016**, *28*, 6631.
- [42] X. Liu, D. Wang, G. Liu, V. Srinivasan, Z. Liu, Z. Hussain, W. Yang, *Nat. Commun.* **2013**, *4*, 2568.
- [43] V. Vanpeene, J. Villanova, A. King, B. Lestriez, E. Maire, L. Roué, *Adv. Energy Mater.* **2019**, 1803947.

- [44] Y. Liu, J. Andrews, F. Meirer, A. Mehta, S. C. Gil, P. Sciau, Z. Mester, P. Pianetta, *AIP Conf. Proc.* **2011**, 1365, 357.
- [45] Y. Liu, F. Meirer, P. A. Williams, J. Wang, J. C. Andrews, P. Pianetta, *J. Synchrotron Radiat.* **2012**, 19, 281.
- [46] J. C. de Silva, A. Pacureanu, Y. Yang, S. Bohic, C. Morawe, R. Barrett, P. Cloetens, *Optica* **2017**, 4, 492.
- [47] P. Cloetens, W. Ludwig, J. Baruchel, D. Van Dyck, J. Van Landuyt, J. Guigay, M. Schlenker, *Appl. Phys. Lett.* **1999**, 75, 2912.
- [48] A. Mirone, E. Brun, E. Guillard, P. Tafforeau, J. Kieffer, *Nucl. Instrum. Methods Phys. Res., Sect. B* **2014**, 324, 41.
- [49] J. Canny, *IEEE Trans. Pattern Anal. Mach. Intell.* **1986**, PAMI-8, 679.
- [50] FeatureJ: Edges.
- [51] C. T. Rueden, J. Schindelin, M. C. Hiner, B. E. DeZonia, A. E. Walter, E. T. Arena, K. W. Eliceiri, *BMC Bioinf.* **2017**, 18.
- [52] R. Xu, L. S. de Vasconcelos, K. Zhao, *J. Mater. Res.* **2016**, 31, 2715.